Simplified Plasmadynamics Model of a Coaxial Self-Field Plasma Accelerator

Rodney L. Burton* and David L. Carroll†
CU Aerospace, LLC, Champaign, Illinois 61822

https://doi.org/10.2514/1.B38923

A simplified plasmadynamics model is presented that examines radial and axial dependence of the current sheet structure of a coaxial quasi-steady self-field plasma accelerator, dominated by electromagnetic forces. Two radial electric field distributions are considered as limiting cases. In the first case, constant current flows between constant-radius electrodes; in the second case, constant current flows between electrodes and also extends downstream of the electrodes. Calculations for Teflon ($C + 2F$) plasma show the distribution of plasma parameters inside the current sheet, as well as terminal values for kinetic efficiency, voltage, and impedance for both E-field distributions. Evaluation of the validity of simplifying assumptions is presented, as is the behavior of previously developed accelerators as interpreted by the model.

Nomenclature

$\boldsymbol{B}$	=	magnetic field, T
C	=	capacitance, μF
$\boldsymbol{E}$	=	electric field, V/m
F	=	force, N
G	=	mass flux, kg/(s · m^2)
G_m	=	mean mass flux, kg/(s · m^2)
h	=	enthalpy, J/kg
I	=	pulse current, A
I_{bit}	=	thrust impulse per pulse mU_e, kg · m/s
j	=	current density, A/m^2
K_Ω	=	Hall parameter correction factor
L'	=	axial inductance gradient dL/dz of accelerator electrodes, H/m
M	=	mean mass of dissociated plasma atoms, kg
$\overline{MW}$	=	mean molecular weight of multiple species plasma
$\dot{m}$	=	mass flow rate, kg/s
n	=	number density of neutral atoms plus ions per m^3
n_e	=	electron number density, electrons/m^3
nfe	=	number of free electrons per heavy particle
P	=	power to heat and accelerate the plasma, W
p, p_e	=	pressure of heavy particles and electrons, Pa
Q^i_{en}	=	electron-neutral impact ionization collision cross section, m^2
R_{oi}	=	electrode radius ratio, r_o/r_i
r	=	radius, m
r_o, r_i	=	outer and inner electrode radii, m
T	=	temperature of neutral atoms and ions, K or eV
T_e	=	temperature of electrons, K or eV
t	=	time, s
t_p	=	pulse length, s
U_e	=	exhaust velocity, m/s
u	=	axial flow velocity, m/s
V_{oi}	=	$\int E_r \, dr$, voltage between outer and inner coaxial electrodes
Z_{em}	=	electromagnetic impedance component 1/4 $L'u_2$ of accelerator, ohms
z_{12}	=	current sheet width, m
α	=	ionization fraction, $0 < \alpha < 1$
ϵ_i	=	ionization potential of atom or ion, V
η_k	=	accelerator kinetic efficiency, $Z_{\text{em}}/(V_{oi}/I) = I^2_{\text{bit}}/2mE_o$
θ	=	electron-to-heavy particle temperature ratio, T_e/T_h
μ_o	=	vacuum permeability, $4\pi \times 10^{-7}$ H/m
ν_c	=	electron–ion Coulomb collision frequency, $n_i Q_{ei} v_{\text{th}}$
ρ	=	plasma mass density, kg/m^3
σ	=	electron electrical conductivity, S/m
Ψ	=	current pulse action integral, $\int I^2 \, dt$, A^2 · s
Ω	=	electron Hall parameter, $eB/m\nu_c$ is equal to $\sigma B/\text{en}_e$
Ω_+	=	ion Hall parameter based on ion-neutral collisions

Subscripts

i, o	=	inner and outer
1, 2	=	current sheet flow entrance and exit conditions

I. Introduction

THE quasi-steady self-field coaxial plasma accelerator has proven to be a superior configuration for several types of electromagnetic accelerators used primarily for space propulsion with solid or gaseous propellants. The coaxial geometry is often preferred over a parallel plate geometry because the lack of sidewalls eliminates that source of thruster erosion and the outer conductor shields a host spacecraft from electromagnetic pulse interference. The development of the coaxial plasma accelerator began with a device called the Marshall gun [1], which injected a puff of gas into the vacuum between coaxial electrodes, with a fast high voltage capacitor bank located at one end. The result was the generation of a magnetohydrodynamic current sheet moving through the injected fill gas, compressing, ionizing, and accelerating the gas to as much as 150 km/s. This moving sheet acceleration mechanism was employed for several types of space thrusters [2,3].

Following the seminal work of Ducati et al. [4], it became evident that an electromagnetic $\boldsymbol{j} \times \boldsymbol{B}$ acceleration mechanism was creating high plasma exhaust velocities in a device called the magnetoplasmadynamic (MPD) arcjet [5]. The MPD arcjet was followed by a quasi-steady acceleration approach developed by Cheng, called the deflagration gun, by analogy with the detonation and deflagration processes in combustible gases [6], thus identifying the Marshall gun and other compressive shock-like accelerators as detonation devices. Since the current distribution in the gas-fed deflagration device is time independent, the accelerated plasma is not compressed but expanded. It was not until decades later that the thrust stand performance of the MPD thruster, as well as the deflagration mode Gas-fed PPT (GFPPT), was determined [7–9].

The Teflon pulsed plasma thruster (PPT) can also be operated in a quasi-steady mode with a coaxial geometry. The propellant is stored in solid form, sublimated, and dissociated near the axis by discharge radiation, and as with gas-fed accelerators, it is expanded into the interelectrode vacuum, thus creating the conditions for quasi-steady

Received 31 May 2022; revision received 26 November 2022; accepted for publication 24 January 2023; published online 10 March 2023.

*Vice President for Research. Associate Fellow AIAA.
†President. Fellow AIAA.

Table 1 Quasi-steady self-field coaxial plasma accelerators ranked by exit velocity

Device	UIUC PPT-11 PPT [10]	U. Rome Mira L MPDT [13]	UIUC GEM MPDT [14]	CUA FPPT [11]	Princeton Benchmark MPDT [7,8]		CUA FPPT [12]	Princeton GFPPT PPT5 [9]	Princeton Benchmark MPDT [8]
Exhaust velocity, km/s	13.5	16.5	22	24	20	40	36	100	175
Propellant	PTFE	PTFE	Gallium	PTFE	Argon	N_2	PTFE	Argon	Hydrogen
Inner electrode	Anode	Cathode	Cathode	Anode	Cathode		Anode	Anode	Cathode
Radius ratio R_{oi}	5	2.6	3.4	5	6		7.5	4	5
$\dot{m}$, g/s	6.7	1.3	4.4	0.8	3.0	4.0	0.85	0.024	0.5
Pulse length, μs	8	500	60	8.7	1000		8.7	8	1000
Pulse current, kA	21.0	11.5	23.6	10.0	17.0	30.0	10.0	6.0	20.0
Peak B field, T	1.1	0.2	1.1	0.5	0.4	0.6	0.6	0.1	0.4
Peak power, MW	6.6	2.0	3.6	3.5	6.8	7.8	4.0	0.13	12.4
Impedance, mΩ	15	8.6	6	38	9.0	9.0	24	21	31
E_r/B, km/s	39	45	27	26 est.	25	25	43 est.	76	88
Maximum EM thrust, N	90	12	96	20	60	180	25	5	82
Thrust efficiency, %	13.7	16	25	6.6	21	36	14	17	57

deflagration. PPTs and magnetoplasmadynamic thrusters (MPDTs) with these solid-to-gas ablative propellant feed characteristics are the PPT-11 [10], the fiber-fed FPPT [11,12], the Teflon MPDT [13], and the gallium electromagnetic (GEM) MPDT [14].

We consider here quasi-steady deflagration-type accelerators for which the current sheet remains at a fixed location on the electrodes. Performance parameters for eight such accelerator types are shown in Table 1, having either anode or cathode inner electrodes. To generate sufficient amplitude of the azimuthal self-magnetic field, these low-impedance devices operate at megawatt power levels, necessitating pulsed operation. Under these high-power conditions the ideal gas approximation is not valid, the plasma is not in thermal equilibrium, and multiple ionized species may be present. Advantageously, however, pre-ionization chambers and exhaust beam neutralization devices are not required.

II. Model of the Plasma Acceleration Process

The approach to predicting the interior structure of an accelerating quasi-steady plasma current sheet employs "a method common in physics: construct a model so simplified as to permit exact mathematical analysis, yet at the same time related as closely as possible to physical reality" [15]. Accordingly we model the current sheet plasma acceleration process using several simplifying but realistic elements [16]. The electromagnetic work done on the accelerator plasma, $\boldsymbol{u} \cdot \boldsymbol{j} \times \boldsymbol{B}$, generates a force (thrust) derived by integration of the $\boldsymbol{j} \times \boldsymbol{B}$ force over the current sheet volume, and it is found to be independent of the current distribution, propellant type, and mass flow rate [17]: $F = (\mu_o/4\pi)I^2[\ell_n(R_{oi}) + C]$, where $0 < 0.75 < C$ is a constant that derives from the current distribution on the downstream ends of the electrodes. In practice the outer-to-inner electrode radius ratio R_{oi} is limited by the requirement to maintain azimuthal current symmetry without discharge spoking. For the simplified model we limit the axial $\boldsymbol{j} \times \boldsymbol{B}$ force density to an interelectrode region $r_i > r > r_o$ for which $C = 0$ and

$$F = \frac{\mu_o}{4\pi} I^2 \, \ell_n(R_{oi}) = \dot{m}(u_2 - u_1) \tag{1}$$

where $\dot{m}$ is the mass flow rate, and u_1, u_2 are the initial and final or exit velocity.

A. Current Pulse Representation

While the current pulse for many gas-fed coaxial plasma accelerators is a nonreversing damped sinusoid, the model adopts an equivalent quasi-steady flat-top current pulse so that the plasmadynamic properties are modeled as constant in time during the pulse. An accelerator pulse such as a typical FPPT current pulse [12] is modeled by a rectangular waveform of pulse length t_p having the same charge transfer $\int I \, dt$ and action integral $\int I^2 \, dt$ (Fig. 1). The quasi-steady assumption is assumed to be valid as long as $t_p \gg t_{accel}$, the time for

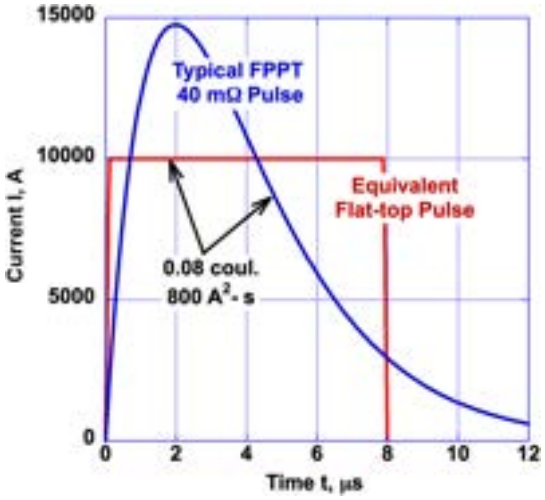

Fig. 1 Typical plasma accelerator current pulse and quasi-steady flat-top pulse with equivalent charge transfer and action integral.

an ion to accelerate through the sheet. The accelerated mass per pulse is m_{bit}, and the instantaneous gas flow rate is $\dot{m} = m_{bit}/t_p$, assumed constant, as is the electromagnetic thrust during the flat-top pulse from Eq. (1). This transformation of the pulse shape generates, for the case of $(1/2)u_2^2 \gg h_1$, a force impulse:

$$\int F \, dt = \frac{\mu_o}{4\pi} \int I^2 \, dt \cdot \ell_n(R_{oi}) \tag{2}$$

where $\int I^2 \, dt \equiv \Psi$ is called the action integral. Because of the equivalence of Ψ for both the experimental and rectangular model pulses, the electromagnetic impulse bit for the model equals that for a thrust stand measurement.

B. Geometry and Mass Flux Distribution

The radial dependence of the electric and magnetic fields plays a major role for $R_{oi} \gg 1$. The azimuthal magnetic field B varies as $1/r$, and the magnetic pressure $B^2/2\mu_o$ varies as $1/r^2$. The electric field component E_r also varies as $1/r$. The radial dependence of other plasma variables is discussed below.

The central electrode in coaxial accelerators can be shorter, longer, or the same length as the outer electrode, creating a variety of radial and axial current density patterns. For simplicity, this model adopts electrodes of the same axial length and constant diameter (Fig. 2), resulting in two cases depending on the location of the current sheet relative to the downstream end of the electrodes. The $z = 0$ plane is physically represented by the position where both electrodes are

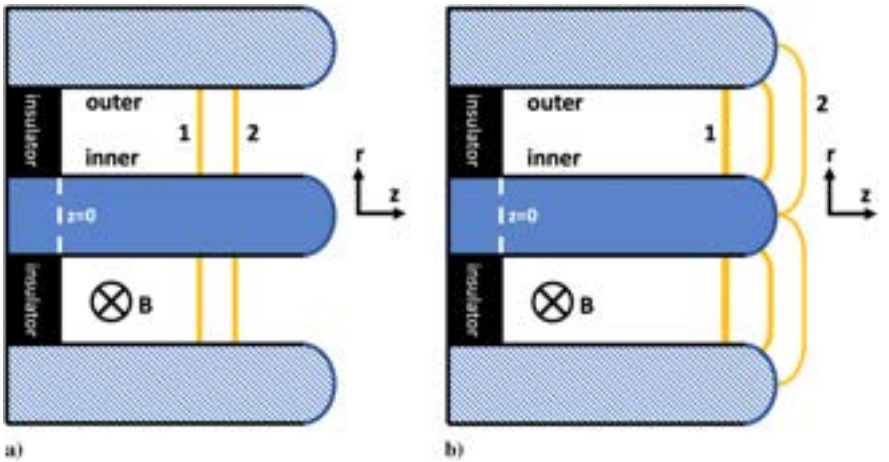

Fig. 2 Coaxial self-field model radial current distributions: a) the current sheet is in a region of constant radius with $E(r)$) constant in z; b) the sheet extends beyond the electrode exit with B and $E(r)$ approaching zero far downstream.

exposed (e.g., at the face of the insulator between the electrodes) so that current can flow. In Fig. 2a the current sheet is shown at an upstream location where the radial electric field is constant in z, and in Fig. 2b the current sheet is shown at the accelerator exit such that E_r falls to zero downstream of the electrodes, resulting in the sheet having a larger axial thickness. With these electrode geometries for simplicity the model assumes purely radial current flowing from the central to the outer electrode ($j_z = 0; j_r > 0$). This approximation is justified since the $j_r B_\theta$ force density is very small in the electrode tip region, is located outside the accelerated plasma flowfield, and does not provide axial acceleration.

The interelectrode plasma is composed of gas particles injected into vacuum as a cold gas to be dissociated and ionized in the current sheet or, in the case of solid propellant, injected by a high-pressure radiation-driven depolymerization, sublimation, dissociation, ionization, and vacuum expansion process. Multiple species can exist, as for the polymer Teflon ($C + 2F$). Instead of calculating the enthalpy, acceleration, and velocity of each species and summing the flow momentum over multiple species with multiple degrees of ionization, the heavy particles are simplified to a single species having the average molecular weight of the injected molecule ($\overline{MW} = 1\ 6.7$ for $C + 2F$). This assumption allows a simple relation $\rho = Mn$ between the heavy particle density n and mass density ρ.

For compound propellants such as Teflon the flow picture is complicated by ion-neutral momentum, charge exchange, and ionization collisions, resulting in a velocity distribution for both ions and neutrals. For the simplified model these details are subsumed under the assumption that all heavy particle velocities are described by a single axial and radial velocity distribution function. Because ions carry little current, most of the pulse current and the $\boldsymbol{j} \cdot \boldsymbol{E}$ energy deposition in the current sheet is absorbed by electrons, which have a Maxwellian distribution and a typical temperature of 1–3 eV. The time between collisions for inelastic electron–ion excitation and ionization collisions is typically 5–30 ns, rapid enough compared to typical particle acceleration times through the sheet of 1–2 μs that parameters such as degree of ionization, electrical conductivity, and plasma internal energy are modeled as being in equilibrium with the local value of electron temperature.

A major model simplification is achieved by assuming that the exit velocity u_2 is independent of radius, which leads to higher accelerator kinetic energy efficiency by reducing distribution losses [18]. This assumption requires that the radial distribution of the injected neutral particle mass flux $G = \rho_1 u_1(r)$ entering the coaxial sheet varies along with magnetic pressure $B^2/2\mu_o$ as $1/r^2$. For both gas-fed and solid-fed coaxial accelerators this heavy particle distribution is injected at hypersonic velocity into the interelectrode vacuum with a velocity u_1 in the $+z$ direction, entering the current sheet as a low-temperature neutral mass flux that becomes rapidly dissociated and ionized.

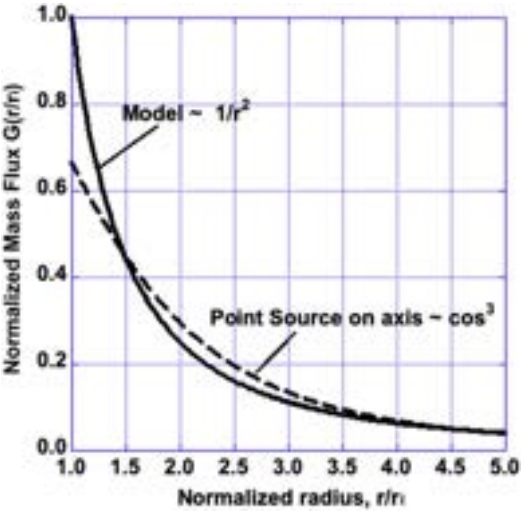

Fig. 3 Correlation of $\cos^3$ law for point source injection and $1/r^2$ dependence for $R_{oi} = 5$ and source at $z_o = 1.8 r_i$.

For gas-fed accelerators the gas injector is a multiple injector "showerhead" design to provide the required $1/r^2$ mass flux distribution. The injected expanded flow is assumed to be shock-free. For coaxial solid-fed space thrusters such as the FPPT (Table 1), the quasi-steady sublimation and dissociation process is approximated as a point source on the axis at ~1.8 central electrode radii upstream from the current sheet, guided by a concave conical interelectrode insulator. The point source creates a quasi-spherical flow of atoms that reaches the radial current disk with a cosine-cubed distribution, which closely approximates the simplified $1/r^2$ function of the model (Fig. 3).

C. Simplified Model Equations and Assumptions

Given the simplifying assumptions of zero axial current with azimuthal symmetry, flow properties are determined by the equations of continuity, momentum, energy, and state, coupled with a generalized Ohm's law. With the plasma fully ionized ($\alpha \sim 1$) and the ion Hall parameter $\Omega_+ \ll 1$, the current sheet model neglects the generalized Ohm's law [19] ion slip term $(1-\alpha)^2(\Omega\Omega_+/B^2)$ $[(\boldsymbol{j} \times \boldsymbol{B}) \times \boldsymbol{B}]$, giving a reduced form for Ohm's law:

$$\boldsymbol{j} = \sigma(\boldsymbol{E} + \boldsymbol{u} \times \boldsymbol{B}) - \frac{\Omega}{B}(\boldsymbol{j} \times \boldsymbol{B}) \tag{3a}$$

where Ω is the electron Hall parameter and σ the electron electrical conductivity. The resulting radial current component is

$$j_r = \sigma(E_r - uB) = \frac{1}{\mu_o}\frac{dB}{dz} \tag{3b}$$

and the axial electric field is

$$E_z = \Omega(E_r - uB) = \Omega j_r/\sigma \tag{4}$$

so that the ion-accelerating field E_z is proportional to j_r. Equation (4) opens the possibility that in regions of large Hall parameter with $E_z > E_r$, the resulting axial accelerating voltage can exceed the interelectrode voltage.

The sheet entrance values of B and E_r are

$$B_1(r, z = 0) = \frac{\mu_o I}{2\pi r} \tag{5}$$

$$E_{r1}(r, z = 0) = \frac{V_{oi}}{r \cdot \ell_n(R_{oi})} \tag{6}$$

where V_{oi} is the applied voltage between the electrodes, neglecting the anode and cathode voltage sheath drops. The sheet entrance field ratio is

$$E_{r1}/B_1 = \left(\frac{V_{oi}}{I}\right)\Big/\left[\left(\frac{\mu_o}{2\pi}\right)\ell_n(R_{oi})\right] \tag{7}$$

where

$$V_{oi}/I \equiv Z_{oi} \tag{8}$$

For coaxial accelerators the electromagnetic power to the ions $P_2 = I^2 Z_{\rm em}$ equals the rate of change of kinetic energy $(1/2)\dot{m}u_2^2$ and produces a thrust force $T = \dot{m}u_2$, so that $Z_{\rm em} = (\mu_o/8\pi)\,\ell_n(R_{oi})u_2$. The power to heat and accelerate the plasma is $P = I^2 Z_{oi}$ and the power ratio $\eta_k = P_2/{\rm P}$ is the kinetic efficiency η_k:

$$\eta_k = Z_{\rm em}/Z_{oi} = \left(\frac{\mu_o}{8\pi}\right)\ell_n(R_{oi})u_2/(V_{oi}/I) \tag{9}$$

The injected heavy particles are at low temperature after vacuum expansion and, lacking a strong heating mechanism, increase in temperature slowly through the current sheet, maintaining a nonequilibrium temperature condition with the hot Maxwellian electrons, identified by the electron/heavy particle temperature ratio $\theta = T_e/T_h$. An estimate of the electron-heavy particle energy equilibration time is made from the Coulomb momentum collision time for a typical discharge temperature of a few eV, multiplied by the ion–electron mass ratio of 31,600 for $\overline{MW} = 16.7$. The resulting equilibration time between electrons and ions requires a 10–100 μs time scale to achieve temperature equilibration, significantly exceeding the $\sim 1 - 2$ μs ion acceleration time through the sheet and maintaining $T \ll T_e$. With the neglect of ion temperature, and the rapid equilibration between ions and neutrals, heavy particle pressure is also neglected compared to electron pressure. Because the sheet structure is insensitive to the heavy particle temperature, the model allows θ in the range $2 < \theta < 5$.

The injected neutral particles rapidly become a partially ionized stream a small distance into the sheet, because of the short electron impact ionization collision time: $\tau_i = (1/(n_n Q^i_{\rm en} v_o)) \sim 1$ ns. The resulting free electrons carry radial current, but also experience a large Hall parameter and resulting $\boldsymbol{E} \times \boldsymbol{B}$ drift, generating an accelerating E_z field by charge separation. At a given radius the one-dimensional inviscid continuity, momentum, and energy equations become

$$\text{Continuity:} \quad \rho u \equiv G = \text{constant} \tag{10}$$

$$\text{Axial momentum:} \quad G\frac{du}{dz} = -\frac{dp_e}{dz} - \frac{B}{\mu_o}\frac{dB}{dz} \tag{11}$$

$$\text{Radial momentum:} \quad G\frac{dv}{dz} = -\frac{dp_e}{dr} \tag{12}$$

$$\text{Energy:} \quad G(dh_o/dz) = -(E_r/\mu_o)(dB/dz) = j_r E_r = j_r^2/\sigma + u j_r B \tag{13}$$

$$\text{Internal energy:} \quad e = h_o - p_e/\rho - u^2/2 \tag{14}$$

where the mass flux is $G(r) = \rho_i u_1 (r_i/r)^2$ and the total enthalpy is $h_o = e + p/\rho + u^2/2$. The internal energy e includes the particle thermal and ionization energies, and it is calculated by assuming plasma equilibrium based on electron temperature. The energy equation is in a form that neglects radiation, discussed below, and separately displays j^2/σ ohmic heating and the $\boldsymbol{u} \cdot \boldsymbol{j} \times \boldsymbol{B}$ electromagnetic work that increases ion kinetic energy.

Radial momentum [Eq. (12)] is neglected in the simplified model. We are interested primarily in the axial velocity, and with the assumption of $j_z = 0$ there is no radial electromagnetic acceleration. Radial velocity resulting from dp_e/dr [Eq. (12)] is discussed in Sec. IV.C.

The electron pressure in the momentum equations is $p_e = n_e k T_e = (nfe) n k T_e$, where $nfe(\rho, T_e)$ [20] is the number of free electrons per heavy particle (Fig. 4). Because the variation in electron pressure is found to be relatively small in the z direction (n_e decreases as T_e increases) the simplified model neglects the gradient term dp_e/dz in the axial momentum equation. Because electron pressure is small compared to $B^2/2\mu_o$, p_e is replaced with a constant mean value $\overline{p_e}$, simplifying the z-momentum relation [Eq. (11)].

The model energy equation neglects radiation loss, based on estimates of contributions from cyclotron, continuum (bremsstrahlung plus recombination), and line radiation. The cyclotron radiation power density P_C [W/m^3] is estimated in the region of maximum B field [21] and compared to the maximum $\boldsymbol{j} \cdot \boldsymbol{E}$ power density, giving $P_C/\boldsymbol{j} \cdot \boldsymbol{E} \sim 10^{-9}$. Because $P_C/\boldsymbol{j} \cdot \boldsymbol{E}$ varies as $1/r^2$ and $B \to 0$ at the exit plane, cyclotron radiation is completely negligible over the current sheet volume.

While PTFE plasmas at pressures above 10^5 Pa are found to have millimeter-scale optical thicknesses [22], current sheet gas dynamic pressures are found to be three orders of magnitude lower and are consequently assumed to be optically thin in the simplified model. Emission coefficients ε [W/m^3/sr] from optically thin equilibrium PTFE plasmas are calculated by Liu et al. [23] as functions of temperature for pressures of 100 and 10,000 Pa, showing that ε is almost independent of temperature above 1 eV. At a pressure slightly below the peak pressures found in the current sheet, the highest

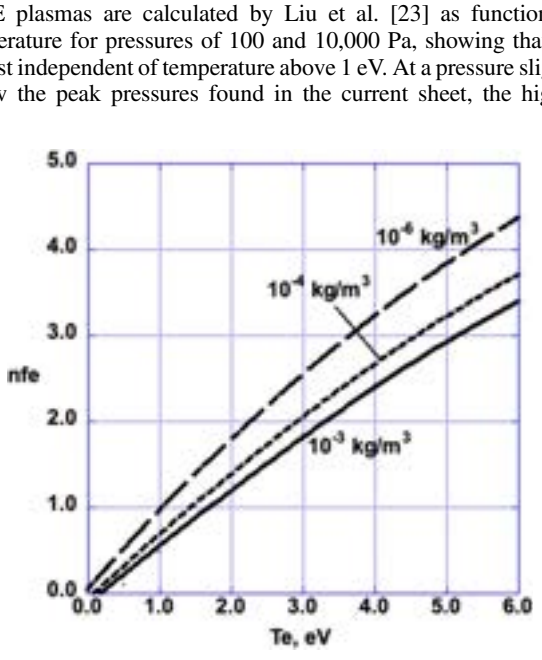

Fig. 4 Number of free electrons per heavy particle $nfe(\rho, T_e)$ for $T_e = 2T_h$ in Teflon plasma for three values of density. Curve-fits are derived from data in Ref. [20].

emissivity comes from line radiation, which is three orders of magnitude higher than recombination (free-bound) radiation and five orders of magnitude higher than bremsstrahlung radiation. The relative continuum and line radiation power densities near the central electrode are $P_{\text{con}}/\boldsymbol{j}\cdot\boldsymbol{E} \sim 10^{-7}$ and $P_L/\boldsymbol{j}\cdot\boldsymbol{E} \sim 10^{-4}$. As both the pressure and $\boldsymbol{j}\cdot\boldsymbol{E}$ vary as $1/r^2$, the neglect of radiation is justified in the simplified model.

Depending on the upstream or downstream current sheet location between the electrodes (Fig. 2), two possible field conservation conditions are assumed to enable calculations of plasmadynamic conditions in the current sheet. For the geometry of Fig. 2a, the current sheet E_r field is constant in z. For the geometry of Fig. 2b, the current sheet field ratio E_r/B is assumed constant in z. For constant E_r, with accelerators having relatively long electrodes, the current sheet is located in a region of constant R_{oi}. The condition of constant E_r/B for accelerators with short electrodes derives from the observation that the B field falls to zero downstream of the electrodes as the E_r field falls to a low value, so that the assumption of constant E_r/B is an approximation of the ratio of these fields downstream of the electrodes. Note that the assumption satisfies the exit boundary conditions of zero j_r, E_r, and B. The assumption of constant E_r/B also provides a simple relation between the gradients of enthalpy h_o and magnetic pressure:

$$G(dh_o/dz) = -(E_r/B)\cdot[d(B^2/2\mu_o)/dz] \tag{15}$$

1. Jump Conditions

Before discussing the internal structure of the current sheet, the continuity, momentum, and energy equations are used to determine jump conditions across the sheet from 1 to 2, with ion temperature $p_i \ll p_e$, and $B_2 = 0$ at the sheet exit plane.

$$\text{The continuity equation gives } \rho_1 u_1 = \rho_2 u_2 \tag{16}$$

The z-momentum equation for constant p_e is integrable:

$$G(u_2 - u_1) = B_1^2/2\mu_o \tag{17}$$

Because we have prescribed the radial variance of mass flux G as $1/r^2$, as does B_1^2 and p_e, the velocity jump $(u_2 - u_1)$ is independent of radius. With reference to conditions at r_i, the inner electrode radius, $G(r) = \rho_i u_1 (r_i/r)^2$ and

$$(u_2 - u_1) = 10^{-7} I^2/(2\pi\rho_i u_1 r_i^2) \tag{18}$$

The energy equation, Eq. (10), is integrable. For constant E_r (Fig. 2a):

$$G(h_{o2} - h_{o1}) = E_r B_1/\mu_o \tag{19a}$$

For constant E_r/B (Fig. 2b) integrating the energy equation gives

$$G(h_{o2} - h_{o1}) = (E_r/B)(B_1^2/2\mu_o) \tag{19b}$$

Having derived the sheet jump conditions from entrance to exit, understanding the sheet structure requires development of the plasmadynamic equations. The generalized Ohm's law components, Eqs. (2–4), with $j_z = 0$ become

$$\text{Constant } E_r\text{:} \qquad j_r = \sigma(E_r - uB); \quad E_z = \Omega(E_r - uB) \tag{20a}$$

$$\text{Constant } E_r/B\text{:} \qquad j_r = \sigma B(E_r/B - u); \quad E_z = \Omega B(E_r/B - u) \tag{20b}$$

Applying the downstream condition $B_2 = 0$ results in

$$\text{Constant } E_r \text{ at } B_2 = 0 \qquad j_{r2} = \sigma E_r; \quad E_{z2} = 0 \tag{21a}$$

$$\text{Constant } E_r/B \text{ at } B_2 = 0\text{:} \qquad j_{r2} = 0; \quad E_{z2} = 0 \tag{21b}$$

For space thruster applications the electromagnetic thrust F_{EM} increases the rate of flow momentum $\dot{m}(u_2 - u_1)$. For an accelerator with the fluid injected along the axis, the electrothermal thrust of propellant injection $F_{\text{inj}} = \dot{m}u_1$ is added to the current sheet thrust $\dot{m}(u_2 - u_1)$, so that the total thrust is the familiar $F = \dot{m}u_2$.

D. Solution Implementation and Variable Dependencies

The assumptions and equations in the previous subsections allow a numerical formulation and integration of the plasmadynamic equations, with the assumption that the local flow parameters are in equilibrium with the electron temperature T_e. The numerical calculation uses axial velocity u as the independent variable. The model is applied here to the CU Aerospace (CUA) FPPT from Table 1 with $u_2 = 36$ km/s, predicting plasma conditions for $r_o > r > r_i$, but not close to the axis where the current is mainly axial. The model therefore inherently matches the experimentally measured exhaust velocity.

With velocity u independent of radius, calculations are performed at $r = 0.49r_o$, the radius at which the local mass flux G equals the mean mass flux $\dot{m}/A$. For a given value of u, density ρ is determined from the continuity Eq. (10). In the first of a three-step process, the electron pressure is initially estimated, allowing estimation of the internal energy $e = h - p_e/\rho$. Given the values of e and ρ the Teflon plasma calculations of Sonoda [20] are used to predict electron temperature T_e as a function of density ρ and internal energy e [GJ/kg] (Fig. 5). By curve-fitting the functions nfe and e [20], two-variable polynomial fits are derived for $T_e(\rho, e)$ and $nfe(\rho, T_e)$, which then determine the electron pressure $p_e = (nfe)nkT_e$, followed by replacing p_e with $\overline{p_e}$. The magnetic field B is then determined from the axial momentum Eq. (11). The resulting incremental changes in u and B then determine a new value of total enthalpy h_o and the plasma internal energy e from Eqs. (13) and (14).

The remaining plasma parameter needed is the electrical conductivity s, which is incorporated by curve-fitting the electrical conductivity calculations of Wang [24] (Fig. 6) for the ion temperature case $\theta = T_e/T_h = 5$ as estimated from the model. Equation (3) then predicts the incremental increase in axial thickness of the current sheet from

$$\Delta z = \Delta B/(\mu_o \sigma(E_r - uB))$$

The electron Hall parameter, needed to calculate E_z from Eq. (4), is written in terms of the electrical conductivity as $\Omega = \sigma B/en_e$. With E_z known, the energy gain for an ion through the sheet is $\int ZE_z\,dz$ [volts] where Z is the ionic charge number, taken as $Z = 1$ for $nfe < 1$, and $Z = nfe$ for $nfe > 1$.

Because the calculation treats the exit velocity as an independent variable, the final kinetic energy of the ions is known, and needs to

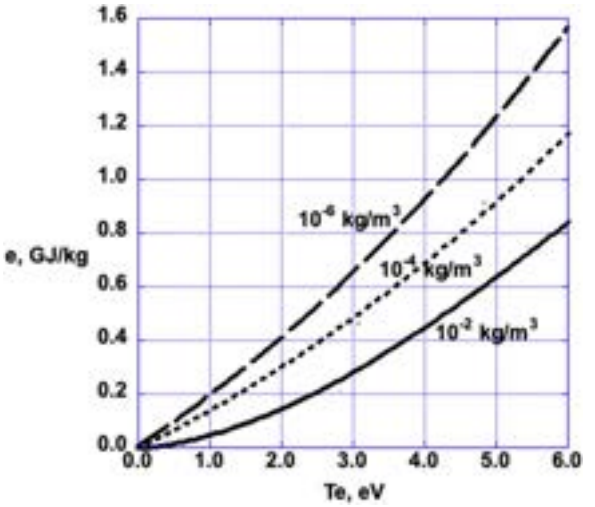

Fig. 5 Internal energy e versus T_e and ρ for $C + 2F$ plasma with electron temperature twice that of the heavy particles for three values of density. Curve-fit from data in Ref. [20].

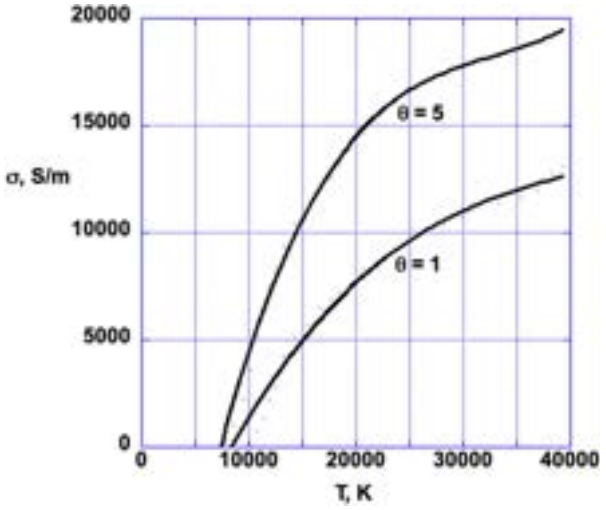

Fig. 6 Teflon electrical conductivity curve-fit from Wang et al. [24] for the cases $\theta = T_e/T_h = 5$ and 1.

agree with the calculation for $\int ZE_z\,\mathrm{d}z$. In general, exact numerical agreement does not occur due to several factors: the assumption of zero axial electron pressure gradient, errors resulting from the curve fits of internal energy, electrical conductivity and degree of ionization, and numerical errors due to finite step size. These factors are accounted for by a single empirical correction factor K_Ω multiplying the electron Hall parameter Ω. The magnitude of the correction depends on u_2 and also on the constant field (E_r or E_r/B) conservation condition, as shown in Table 2. Note that $K_\Omega \approx 1$ at the higher values of u_2, indicating a small correction.

The model inherently incorporates radial variations in the plasma properties. Because B^2 and (by assumption) G both vary as $1/r^2$ from Eqs. (11) and (12), a velocity increase $du = -(dB^2/2\mu_o)/G$ is independent of radius. Both j_r and E_r vary as $1/r$ so the total enthalpy increase $(h_{o2} - h_{o1})$ is also independent of radius and the same is assumed true for the electron temperature: $T_e = T_e(z)$. With T_e and $\sigma(T_e)$ independent of radius, the electron Hall parameter $\Omega = \sigma B/en_e$ scales as $B/n_e\tilde{r}$. From Eq. (7) the accelerating electric field E_z is independent of r. Because the ionic charge Z_i depends on the total enthalpy h_o, a quantity independent of radius, the ion energy equation

$$m_i(u_2^2/2 - u_1^2/2) = e\int Z_i E_z\,\mathrm{d}z = eV_{12} \tag{22}$$

is independent of r, making the current sheet acceleration length Δz also independent of r (Fig. 2). The radial dependences of the principle plasmadynamic variables are summarized in Table 3.

Table 2 Hall parameter correction factor K_Ω for $R_{oi} = 5$, to equalize final kinetic energy and sheet acceleration voltage for $p_{e2} - p_{e1} = 0$

Exit velocity u_2, km/s	12	24	36	48
K_Ω for constant E_r	0.710	0.878	0.982	0.991
K_Ω for constant E_r/B	0.630	0.948	0.984	1.018

Table 3 Radial dependence of current sheet variables

Variable	Radial dependence
ρ, n, n_e, G, p, p_e	Varies as $1/r^2$
E_r, B, j_r	Varies as $1/r$
$u, h, T_e, E_r/B, \sigma, E_z, \eta_k$	Independent of r
Ω	Varies as r

E. Modified Minimum Principle

Still to be specified is the accelerator interelectrode voltage V_{oi}, which for a given current I determines the conservation conditions E_r or E_r/B. Referring to Table 1, a typical arc impedance, including the effect of electrode sheaths, is 15–20 mΩ, suggesting a low value of voltage for a current on the order of 10 kA. However, to prevent j_r and j_rB reversal within the sheet, Ohm's law, Eq. (3), requires $E_r \geq uB$, equivalent to placing a minimum value on V_{oi}.

In 1932, Steenbeck hypothesized a "minimum principle" that a cylindrical arc column with constant current will operate such that the axial electric field is minimized [25–27]. More recently the scientific basis for Steenbeck has been questioned [28,29]). Could a possible approach to selecting V_{oi} be a modified form of the Steenbeck minimum principle, configured for the radial current case instead of the axial current geometry of Steenbeck? Invoking Steenbeck runs into the difficulty that the Steenbeck arc plasma has zero flow velocity, while the self-field accelerator has a uB term in Ohm's law, which can result in zero current density j_r and an infinite axial width from $dz = dB/\mu_o j_r$.

For the simplified model the Steenbeck infinite width problem is avoided by selecting an empirically based axial current sheet width (Table 1), which then uniquely defines the voltage V_{oi} and the field conservation conditions. The selected widths are $z_{12} = 1.5r_o$ for constant E_r and $z_{12} = 3.0r_o$ for constant E_r/B. Such restrictions require only a few percent increase in E_r above $E_r = uB$, with the result that the discharge operates close to, but not at, the minimum voltage.

The first-order equations can now be solved numerically, using velocity u as the independent variable, and velocity-marching from u_1 to u_2 ($B = B_1$ to $B_2 = 0$), with a mean atomic weight of 16.7. The calculation is checked by verifying that the integrated radial current density equals the total accelerator current, with the factor K_Ω used to satisfy the energy equation, Eq. (19).

III. Model Results

A. Results from Simplified Current Sheet Model

Results are given for Teflon plasma and $R_{oi} = 5.0$ using typical values of electromagnetic thrust and pulse length t_p (Fig. 1) [11]. The initial value $u_1 = 3000$ m/s is estimated for conditions where Teflon is sublimated on axis at $\sim 10^5$ Pa to a plasma temperature of ~10,000 K and expanded into vacuum. The flux density ρu is the mean value $G_m = (m/t_p)/(\pi(r_o^2 - r_i^2))$, which occurs at the mean radius $r_m/r_o = 0.49$.

The position of the sheet exit plane, where radial current density j_r becomes negligible, is chosen as a multiple of the radius r_o of the outer electrode. For $E_r =$ constant, the sheet thickness of $1.5r_o$ is set by a few percent correction to the mean mass flux G_m. For $E_r/B =$ constant, the sheet thickness is sensitive both to G_m and to the value of E_r/B, which is set to 38 km/s, 2 km/s higher than u_2, while G_m is adjusted to set sheet thickness at $3r_o$ according to the current pattern shown in Fig. 2.

Current sheet plasmadynamics are primarily determined by the model electric and magnetic field distributions. The net radial electric field $(E_r - uB)$ and axial field E_z are plotted for constant E_r (Fig. 7) and for constant E_r/B (Fig. 8), at $r_m/r_o = 0.55$. The plots of constant E_r/B are truncated at $\Delta z/r_o = 1.5$, where u has reached 99.3% of u_2. As noted in Fig. 2, the $z = 0$ plane is physically represented by the position where both electrodes are exposed (e.g., at the face of the insulator between the electrodes) and where radial current can begin to flow.

The electric field distributions of the two cases are distinctly different. While for both cases the E_z field component always exceeds $(E_r - uB)$, for constant $E_r(z)$ the accelerating E_z field extends through the sheet, reaching its highest value near the sheet exit where $B = 0$. For constant E_r/B the E_z field is initially four times higher (32 kV/m vs 8 kV/m), with 95% of exit velocity being reached at only 14% of the sheet thickness, with the $\boldsymbol{E}$ fields falling to a low value in a short distance.

Velocity distributions for these two cases are shown in Fig. 9a, with the corresponding B field distributions in Fig. 9b. For constant E_r/B

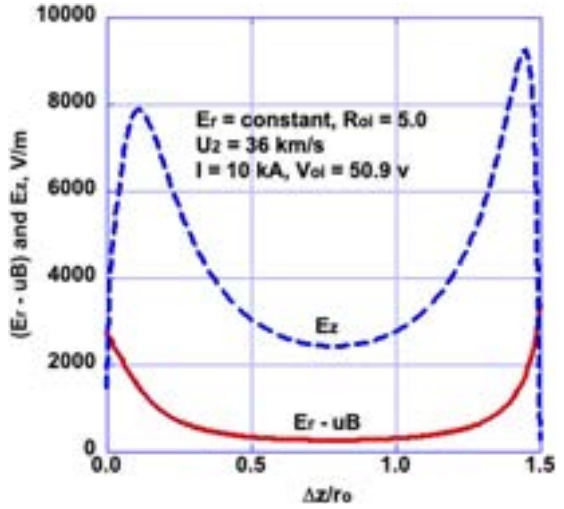

Fig. 7 $(E_r - uB)$ and E_z at $r/r_o = 0.49$ for constant $E_r(z)$ at $u_2 = 36$ km/s ($u = 95\%$ of u_2 at 97% of sheet width).

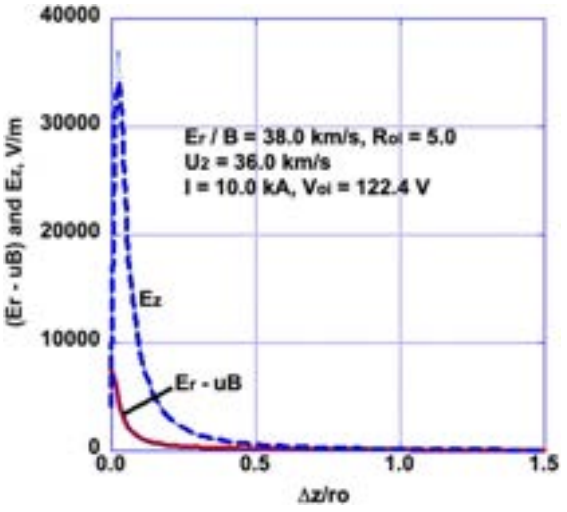

Fig. 8 $(E_r - uB)$ and E_z at $r/r_o = 0.49$ for constant E_r/B at $u_2 = 36$ km/s ($u = 95\%$ of u_2 at 14% of sheet width).

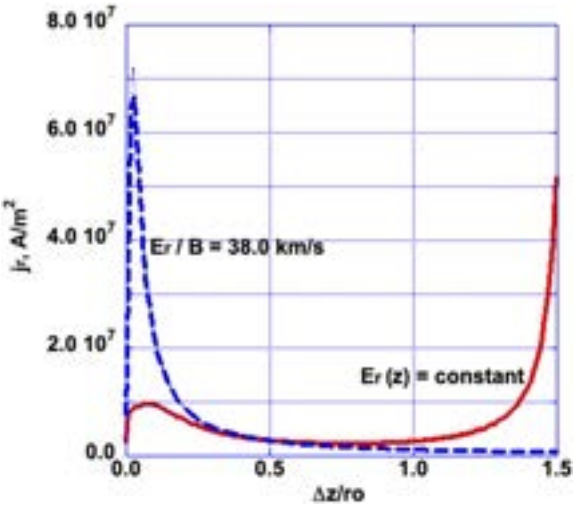

Fig. 10 Radial current density j_r versus axial distance for constant $E_r(z)$ and $E_r/B = 38.0$ km/s for $u_2 = 36$ km/s case.

most of the acceleration occurs near the sheet entrance at high magnetic field. For constant $E_r(z)$ the slope of the velocity profile is approximately uniform across the sheet, which has half the width of the constant E_r/B case.

The current density j_r [A/m^2] and $\boldsymbol{j} \times \boldsymbol{B}$ force density $j_r B$ [N/m^3] are plotted versus axial distance in Figs. 10 and 11. For constant $E_r(z)$ the current density is relatively uniform across most of the sheet and then peaks as B approaches 0, due to an increase in electrical conductivity σ and the simultaneous disappearance of the back electromotive force (EMF) uB. For constant E_r/B the current density peaks rapidly at the sheet entrance plane, accompanied by ohmic heating that quickly raises the electron temperature and electrical conductivity σ, after which σ remains relatively constant throughout the sheet while j_r falls to a low value as E_r and B decrease simultaneously.

The axial $\boldsymbol{j} \times \boldsymbol{B}$ volume force density [N/m^3] (Fig. 11) behaves in a similar way to j_r. For constant $E_r(z)$, the $j_r B$ distribution is approximately uniform across the sheet. For constant E_r/B the force density peaks in the high B field region and then falls rapidly to a very low value at the exit plane.

The interior ohmic heating j_r^2/σ and electromagnetic work uj_rB for the two EM field conditions are plotted versus $\Delta z/r_o$ in Figs. 12 and 13, again following distinctly different profiles. The constant E_r

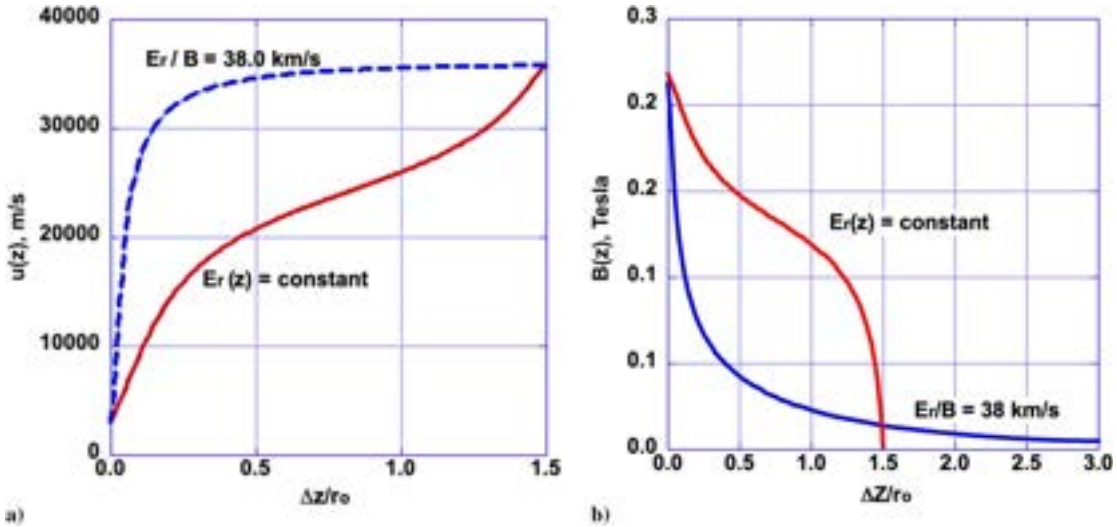

Fig. 9 a) Velocity profiles for constant $E_r(z)$ and $E_r/B = 38.0$ km/s at $u_2 = 36$ km/s, $R_{oi} = 5.0$. b) $B(z)$ profiles for constant $E_r(z)$ and $E_r/B = 38.0$ km/s at $u_2 = 36$ km/s.

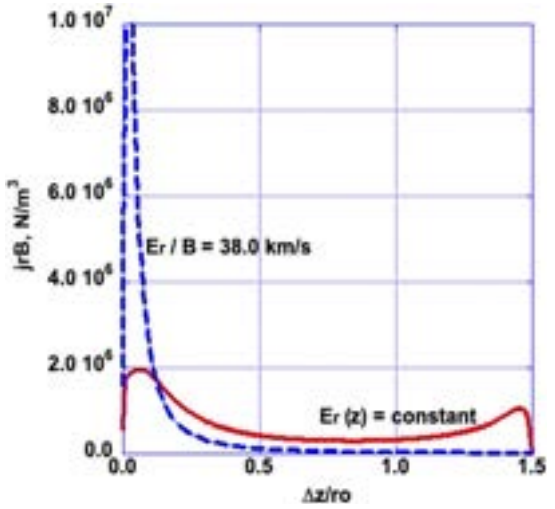

Fig. 11 Axial force density j_rB versus axial distance for constant $E_r(z)$ and $E_r/B = 38.0$ km/s for $u_2 = 36$ km/s case.

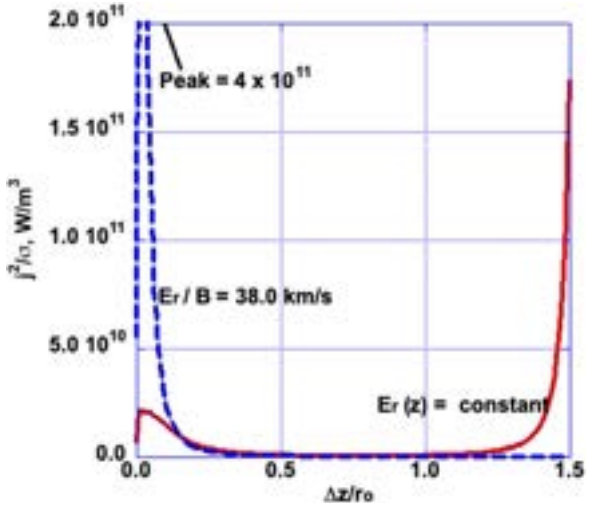

Fig. 12 Ohmic heating j_r^2/σ for $u_2 = 36$ km/s.

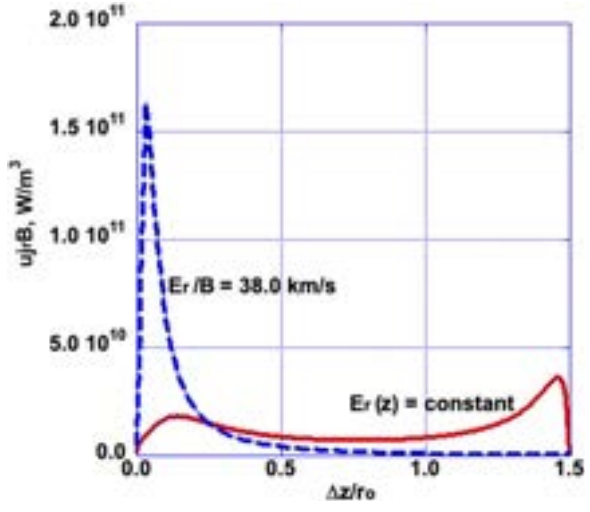

Fig. 13 Electromagnetic work uj_rB for $u_2 = 36$ km/s.

case distributes j^2/σ and uj_rB across the sheet. For constant E_r/B the two parameters are concentrated at the sheet entrance.

Figures 14–16 plot T_e, nfe, and σ for $u_2 = 36$ km/s for $R_{oi} = 5.0$. For constant E_r/B the electron temperature rises rapidly

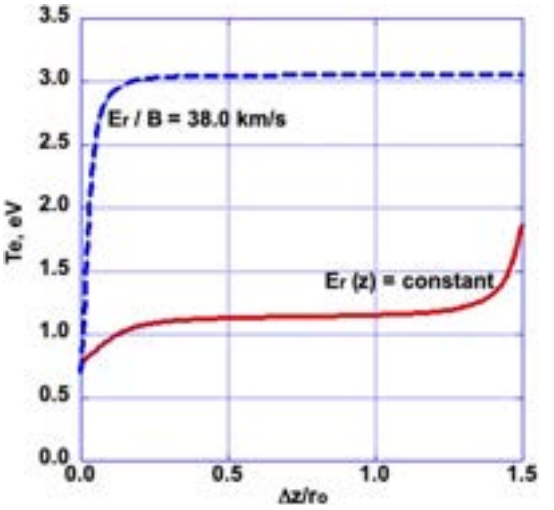

Fig. 14 Electron temperature T_e,eV, $u_2 = 36$ km/s and $R_{oi} = 5.0$.

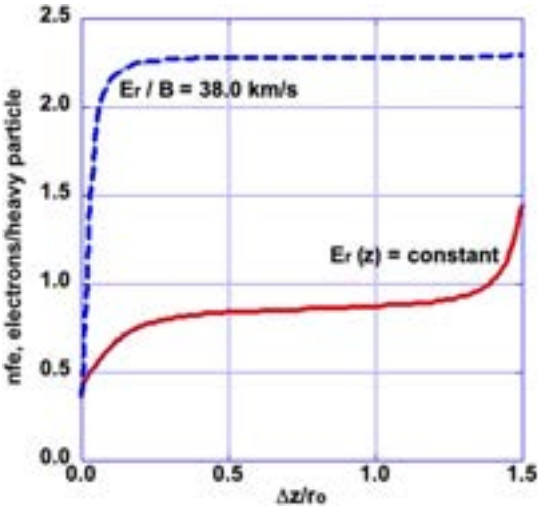

Fig. 15 Number of free electrons per heavy particle, $u_2 = 36$ km/s and $R_{oi} = 5.0$.

to $T_e > 3$ eV. The degree of ionization for the Teflon plasma is expressed as the number of free electrons per heavy particle $nfe(\rho, T_e)$ [20], and rises rapidly to $nfe \sim 2.2$, and the electrical conductivity rises to ~18,000 S/m, values that hold constant across the current sheet. Under these conditions the effect of neutrals on the acceleration process will be negligible. For constant $E_r(z)$ these three quantities are distributed completely differently (Figs. 14–16), being constant at a reduced level across the current sheet and then rising as the accelerated plasma approaches $B = 0$. The electron temperature reaches $T_e = 1.8$ eV, nfe exceeds full ionization at $nfe = 1.4$, and the electrical conductivity reaches 15,000 S/m.

B. Kinetic Efficiency

The ideal accelerator kinetic energy efficiency η_k is expressed as the kinetic power of the accelerated plasma per unit input power, neglecting electrode voltage sheaths and the relatively small kinetic energy of injection:

$$\eta_k = \frac{1}{2}\dot{m}u_2^2/IV_{oi} \tag{23}$$

where $V_{oi} = \int_i^o E_r \, dr$ is the interelectrode voltage without electrode sheath drops. For constant E_r/B the kinetic efficiency can be expressed analytically. Writing the electromagnetically generated kinetic power as I^2Z_{em} and the total input power between electrodes as I^2Z_{oi}, then

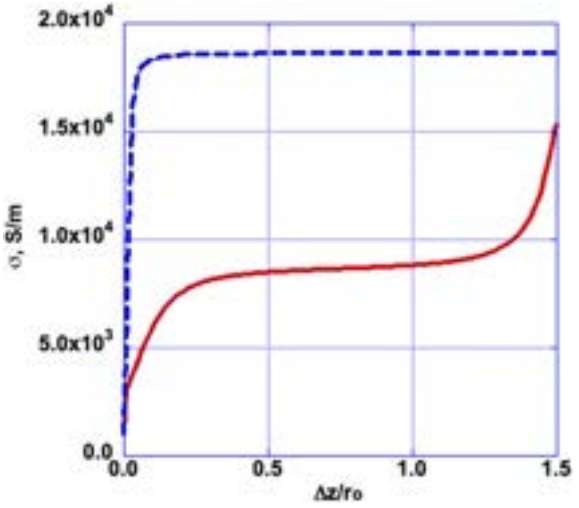

Fig. 16 Electrical conductivity, S/m.

$$\eta_k = Z_{\rm em}/Z_{oi} = 1/4 \cdot L' u_2/(V_{oi}/I) = u_2/(4E_{r1}/B) \qquad (24)$$

The minimum value of E_r/B is u_2 and the maximum value of η_k is 1/4 (25%) for constant E_r/B, independent of R_{oi}.

For constant $E_r(z)$ the minimum value of E_r/B is less than u_2 and the efficiency is significantly higher than for constant E_r/B. The increase in efficiency with u_2 is shown in Table 4. Because both the accelerating force and the radial electric field are proportional to the geometric term $\ell_n[R_{oi}]$, the kinetic efficiency η_k is independent of R_{oi}.

The accelerating voltage V_{12} is given by the integration of the axial E_z field: $\int E_z \, dz = V_{12}$. The ratio between V_{12} and the interelectrode voltage V_{oi} is show in Table 5. The voltage ratio increases over the range of exit velocities, and significantly exceeds the interelectrode voltage for constant E_r, consistent with higher efficiency for the constant E_r field condition.

Table 5 gives a wide range of values for V_{12}/V_{oi}, the ratio of ion accelerating voltage to electrode terminal voltage that depends on the E_r boundary condition. The conventional expression for the efficiency of a plasma accelerator is the ratio of the power in the exhaust beam to the electrical input power: $\eta_k = (1/2)\dot{m}U_e^2/P$. In terms of the voltages V_{oi} and V_{12}, $\eta_k = (e\dot{m}/MI)V_{12}/V_{oi}$, giving $V_{12}/V_{oi} = \eta_k(MI/e\dot{m})$. The quantity $MI/e\dot{m}$ is the ratio of radial current to ion beam current, where ion beam current equals axial electron current since $j_r = 0$. The mass flow rate is $F_{\rm em}/U_e$ giving $\dot{m} = \frac{\mu_o}{4\pi} I^2 \ell_n(R_{oi})/U_e$, resulting in $V_{12}/V_{oi} = \eta_k[MU_e/(e(\mu_o/4\pi))I \cdot \ell_n(R_{oi}))]$. The voltage ratio is proportional to the kinetic efficiency multiplied by the factor in brackets, indicating that conditions for $V_{12}/V_{oi} > 1$ can occur in the acceleration of a high-MU_e plasma with relatively low current.

Table 4 Kinetic efficiency η_k versus u_2 for constant E_r

u_2, km/s	12	24	36	48
$\eta_k = \frac{1}{2}\dot{m}u_2^2/IV_{oi}$	0.346	0.485	0.570	0.602

Table 5 Ratio V_{12}/V_{oi} of induced accelerating voltage to interelectrode voltage versus u_2

Exit velocity u_2, km/s	12	24	36	48
V_{12}/V_{oi} (constant E_r)	0.42	1.24	2.20	3.10
V_{12}/V_{oi} (constant E_r/B)	0.26	0.59	0.91	1.31

IV. Discussion

The simplified model of a quasi-steady coaxial self-field accelerating current sheet provides insight into the sheet plasmadynamics, but in the quest for simplicity also ignores important physics issues. These limitations and weaknesses of the simplified model are examined in the subsections below. Rough estimates of the potential impact of those physics issues on the simplified model predictions are presented in Sec. III.

A. Importance of Hall Effect

For the self-field coaxial accelerator with applied radial electric field E_r, the model shows the existence of a strong axial electric field E_z, independent of radius, that is not applied but is induced by the Hall effect (Fig. 17) to accelerate the ions. The axial ion flux and resulting current is counterbalanced by an equal electron flux, resulting in zero axial current and eliminating the need for exhaust beam neutralization as required for ion and Hall effect thrusters. From Eq. (4) the accelerating axial electric field is proportional to the Hall parameter and the radial field by $E_z = \Omega(E_r - uB)$, where the field $(E_r - uB)$ varies is $1/r$ and Ω is proportional to r. Thus the Hall effect plays a major role in plasma acceleration in coaxial self-field devices.

B. Neglect of Axial Pressure Gradient

The simplified model employs a mean value for p_e, neglecting the effect of ∇p_e on plasma motion. The calculated and mean values of p_e for $R_{oi} = 5.0$ are shown for $u_2 = 36$ and 48 km/s in Fig. 18. The axial dp_e/dz term is generally small compared to $j_r B$ throughout the current sheet width and has been neglected.

C. Ion Divergence from Axis by Radial Pressure Gradient

While the assumption $j_z = 0$. leads to the assumption radial velocity $v = 0$ by neglect of the radial momentum Eq. (12), the radial flow velocity contribution from dp_e/dr can be estimated from model results. The radial gradient is estimated using the mean value of electron pressure (Fig. 18). Since the model adopts T_e independent of radius and $p_e \sim 1/r^2$, for conditions equal to the mean mass flux G_m for $R_{oi} = 5$, and using typical sheet values for $u_2 = 36$ km/s with $\Delta z = 2.8$ cm, $\Delta v \sim -(1/G_m)(dp_{\rm em}/dr)\Delta z \sim 800$ m/s. The resulting flow angle to the axis at the exit plane is ($\theta_m = \arctan(800/36{,}000) \sim 1.3°$, implying a small ∇p_e flow divergence for this coaxial accelerator. The gradient varies as $1/r$ so that the steepest divergence angle near the central electrode is $\theta \sim 3°$.

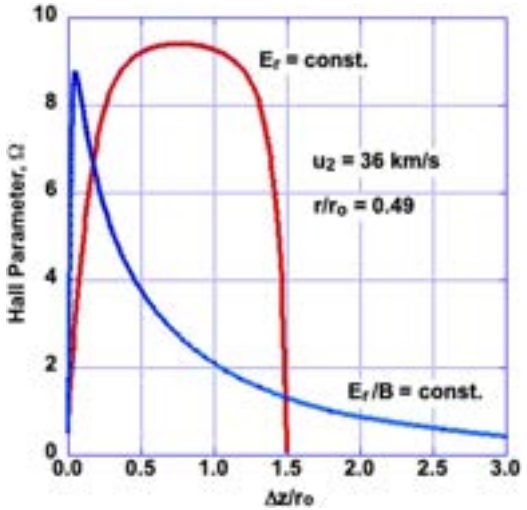

Fig. 17 Electron Hall parameter Ω for constant E_r and constant E_r/B, at $r/r_o = 0.49$, where mass flux equals the median value. Ω is proportional to radius.

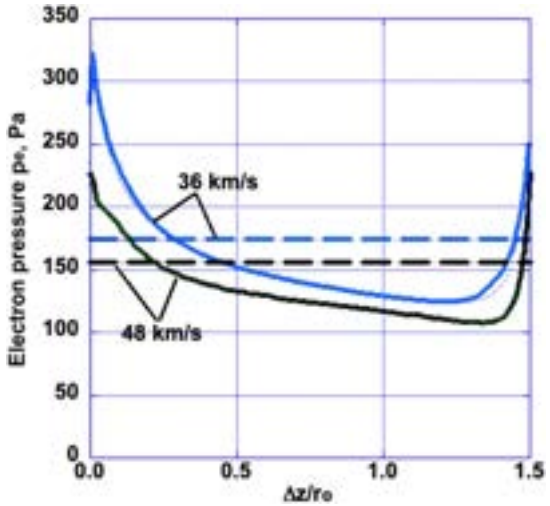

Fig. 18 Electron pressure $p_e(z)$ (solid lines) and mean electron pressure $\overline{p_e}$ (dashed lines) at $r = 0.49r_o$ for 36 and 48 km/s.

D. Ion Hall Parameter

Particle models of self-field accelerators have been proposed previously using E_r and B fields for which the ion Larmor Radius is greater than the thruster dimensions, so that heavy ions (e.g., xenon, argon) in the radial E field with central cathode and insufficiently high B field can execute cycloidal motion ($\boldsymbol{E} \times \boldsymbol{B}$ drift) and collide at the thruster axis [30]. For the reverse polarity, heavy ions can gyrate from a central anode outward and strike the cathode [31]. The present model differs in that the dominant electric field is axial, not radial. Gyrational motions occur in a region of strong magnetic field gradient, and in some cases can be interrupted by ion-neutral (i-n) collisions. These i-n collisions occur at low velocity near the current sheet entrance with a mean free path of a few millimeters, lengthening as the particle densities decrease and the Larmor radius increases, resulting in a relatively small radial drift within the sheet. Unlike the radial drift caused by electron pressure, the direction of the $\boldsymbol{E} \times \boldsymbol{B}$ drift depends on electrode polarity and accelerator type (Table 1).

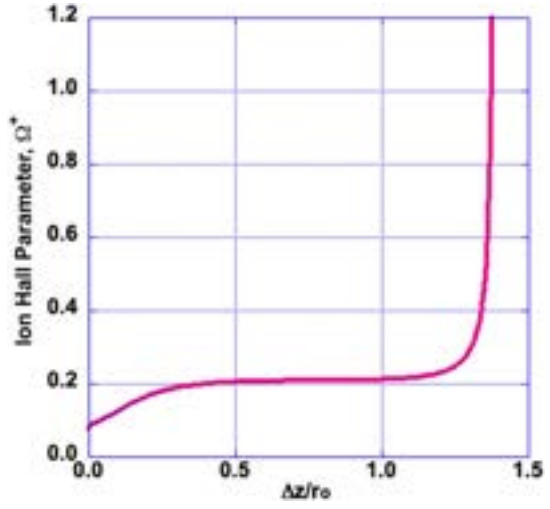

Fig. 19 Ion Hall parameter versus $\Delta z/r_o$ for constant E_r, $u_2 = 36$ km/s and $R_{oi} = 5.0$ at the mean flux radius, with $nfe = 1$ at $\Delta z/r_o = 1.4$.

Before full ionization is achieved in the current sheet the ion motion can be described in terms of the ion Hall parameter, written in terms of an ion-neutral elastic collision frequency $\nu_{+n} = n_n Q_{+n} u$, where $n_n = n(1 - nfe)$. The ion Hall parameter is then $\Omega_+ = (\omega_B/\nu_{+n}) = (e/\rho u Q_{+n})(B/(1 - nfe))$ where $\rho u = G$, the mass flux. A typical variation of ion Hall parameter is shown in Fig. 19 for constant $E_r(z)$, $u_2 = 36$ km/s and $R_{oi} = 5.0$ at the mean flux radius for an expected value of Q_{+n}.

E. Kinetic Efficiency Including Voltage Sheath Drops

Electrode sheath voltage drops can significantly reduce kinetic efficiency, particularly at low u_2. Assuming that the magnitude of each sheath drop is on the order of the mean atomic ionization potential, approximately 15 V, the efficiencies in Table 4 are modified by including in V_{oi} an additional contribution of 30 V from the inner and outer electrode voltage sheaths. The kinetic efficiency η_k decreases when electrode sheaths are included, but benefits from increasing both u_2 and R_{oi} (Table 6). Kinetic efficiency also benefits from increasing current and hence V_{oi}.

F. Local Variation in Kinetic Efficiency

The value of kinetic efficiency $\eta_k(z)$ varies through the sheet and is independent of r:

$$\eta_k(z) = (uj_rB/j_rE_r) = u/(E_r/B) \tag{25}$$

where $\eta_k(z)$ is proportional to u/B for constant $E_r(z)$. For $u_2 = 36$ km/s (Fig. 20) the local efficiency exceeds 90% midway through the current sheet, a region where current density, ohmic heating, and ionization rates are low.

From Eq. (13) the local efficiency $\eta(z)$ can also be defined as

$$\eta_\ell(z) = \frac{uj_rB}{j_r^2/\sigma + uj_rB} = \frac{1}{1 + j_r/\sigma uB} = \frac{R'_M}{R'_M + 1} \tag{26}$$

where R'_M is the local magnetic Reynolds number $R'_M = \sigma uB/j_r \approx \mu_o \sigma u \Delta z'$. Since $\eta_\ell \to 1$ for $R_{\ell M} \gg 1$, efficient sheet conditions are reached for high values of σ and u, and low current density j_r, in turn implying low $(E_r - uB)$ and long electrodes. For a self-field accel-

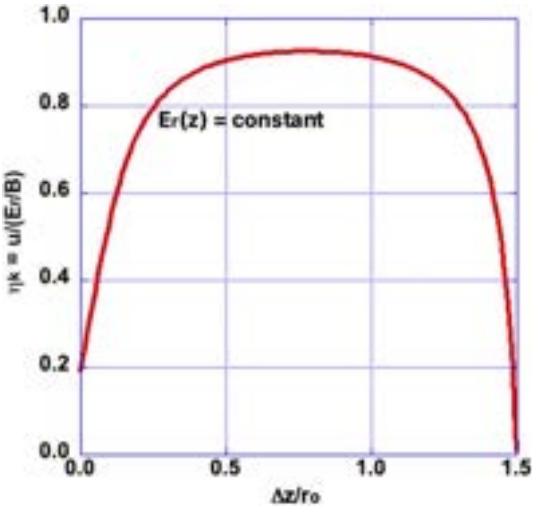

Fig. 20 Local value of kinetic efficiency for $u_2 = 36$ km/s, $R_{oi} = 5.0$.

Table 6 Variation of kinetic efficiency η_k with u_2, including 30 V electrode sheath drop

u_2, km/s	12		24		36		48	
R_{oi}	5.0	7.5	5.0	7.5	5.0	7.5	5.0	7.5
$\eta_k = \frac{1}{2}\dot{m}u_2^2/I(V_{oi} + V_{\text{sheath}})$	0.167	0.186	0.277	0.303	0.358	0.387	0.410	0.438

erating sheet it would therefore be useful to configure the coaxial electrodes to achieve small values of $(E_r - uB)$. If it is assumed that E_r can be tailored by varying R_{oi} so that $E_r = KuB$, where K is a constant of proportionality, then $\eta(z) = (1/K)$ and approaches 1 as $K \to 1$, subject to limitations on sheet width as $j_r \to 0$. Varying R_{oi} by flaring the outer accelerator electrode to improve efficiency was investigated numerically by King [32], who also identified the advantage of increasing accelerator length.

Note that the shape of the curve for η_k in Fig. 20 is similar to that of the electron Hall parameter Ω in Fig. 17 for constant E_r. The ratio η_k/Ω can be formulated as $(nfe) \cdot n^+u/(\sigma E_r)$, which becomes constant for constant T_e as is approximately the case in Fig. 14.

G. Effect of Multiple Species

Although the model assumes a monatomic plasma, the application to a Teflon $(C + 2F)$ plasma necessarily implies multiple species with multiple degrees of ionization (Table 7). For $u_2 = 36$ km/s, $R_{oi} = 5.0$, and constant $E_r/B, T_e > 3.0$ eV and $nfe > 2$ over most of the current sheet, while for constant E_r, $T_e < 1.5$ eV and $nfe < 1$ over most of the current sheet (Figs. 14 and 15). The results imply that the constant E_r/B plasma is mostly singly and doubly ionized, while the constant E_r plasma is singly ionized carbon with partially ionized fluorine over most of the current sheet. We would therefore expect, because all ions are accelerated by the same E_z field, that the accelerator exhaust velocity distribution would include carbon ions at $u_{C+} > 36$ km/s, fluorine ions at $u_{F+} < 36$ km/s, and even slower fluorine and carbon ions that were ionized near the exit region.

H. Mach Number of Plasma

The entire acceleration process through the sheet is predicted to be completely supersonic, so that the flow does not pass through an MPD choke point, avoiding the choking singularity at Mach 1 [33]. The sound speed is estimated using the approximation approach of Ahlborn [34] derived from the velocity at the Jouguet point on a $p - V$ diagram, which is shown to be a reasonably close approximation to the plasma sonic velocity. Flowing through the sheet with $u_2 = 24$ km/s, the resulting Mach number for the case of constant E_r starts at 1.9, increasing to 9.1 at the exit (Fig. 21). The Mach number for the case of $u_2 = 24$ km/s and constant E_r/B starts at 2.1, increasing to 6.3 at the exit, slightly higher than the constant E_r case.

Table 7 Components of dissociated and ionized Teflon, $\overline{MW} = 16.7$

MW	12			19		
Species	C	C^+	C^{++}	F	F^+	F^{++}
ε_i, eV	11.26	24.38	47.89	17.42	34.97	62.71

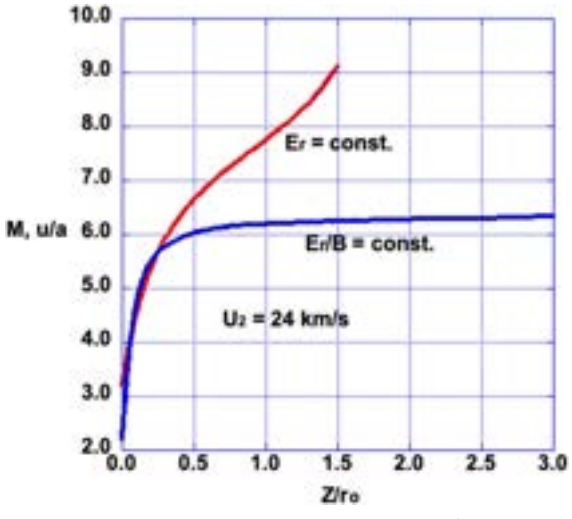

Fig. 21 Mach number at $u_2 = 24$ km/s.

I. Current Sheet Tilt

In the absence of ion neutral collisions, the ion is accelerated by the vector addition of the axial electric field E_z and the net radial field $(E_r - uB)$. The angle $\theta = \arctan(1/\Omega)$ of the electric field vector to the z axis is >0 everywhere in the flowfield and is plotted in Fig. 22 for $u_2 = 36$ km/s at the mean flux radius. For this case the time-averaged value is $\overline{\theta} = (1/\Delta t)\int_0^{\Delta t} \theta \, dt = 10.7$ degrees for a total acceleration time $\Delta t = 1.56$ μs. The value of $\overline{\theta}$ decreases with increasing radius because Ω is linear in r, so the flow divergence is reduced at larger radii.

Since the $\boldsymbol{E}$ field, according to the model, creates a radial ion velocity, Eq. (12) predicts the existence of an axial current component, in contradiction to the model assumption of purely radial current. The radial component combines vectorially with the axial component to tilt the current sheet [35]. For an accelerator with central anode the result is a divergence in the exit flow, caused by a backward tilt in the current sheet (Fig. 23). The implication is that a length extension of the central anode is needed to keep the acceleration process in the constant E_r mode.

J. Role of Neutrals

The model ignores the role of neutral particles in the acceleration process, a neglect that is more important for the reduced ionization levels of the constant E_r case. The ion slip current density term $-(1 - \alpha)^2\Omega\Omega_+ j_r$ was neglected in the generalized Ohm's law, and this term is evaluated (Table 8) using model results for constant E_r after evaluating the ion Hall parameter Ω_+ with a calculated ion-

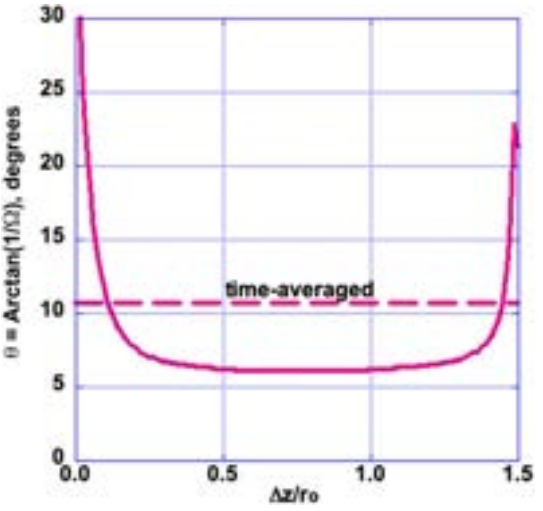

Fig. 22 Angle $\theta = \arctan(1/\Omega)$ of net electric field vector at $r_m = 2.45r_o$ and time-averaged θ to the z axis for $u_2 = 36$ km/s and $R_{oi} = 5.0$.

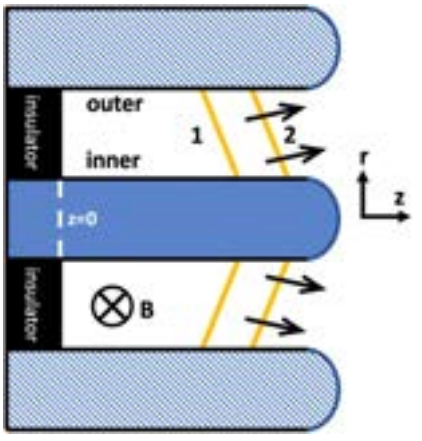

Fig. 23 Coaxial self-field model radial current distributions with a tilted current sheet.

Table 8 Constant E_r effect of ion slip on radial current density at $u = u_2/2$ for $R_{oi} = 5.0$

Exit velocity u_2, km/s	12	24	36	48
Degree of ionization $\alpha = nfe$	0.52	0.61	0.77	0.99
Electron Hall parameter Ω	0.7	3.1	8.4	16.6
Ion Hall parameter $\Omega+$	0.15	0.28	0.20	28.0
Slip factor = ion slip current/j_r	−0.02	−0.13	−0.09	−0.01

neutral collision frequency. The calculation was performed at the mean mass flux radius $r_m/r_o = 0.49$ at a velocity of $u_2/2$. For constant E_r the effect of ion slip on radial current, neglected in the model, peaks at $u_2 = 24$ km/s and falls to zero at 48 km/s and higher velocities where $nfe = \alpha \approx 1$. The net effect is a reduction in radial current of up to 13%.

A more serious deficiency in the simplified model occurs from implicitly assuming that the ions and neutrals act as a single fluid with common velocity components u and v. As neutrals enter the sheet, a fraction are rapidly ionized (Fig. 14) and accelerated by the induced E_z field to a higher axial velocity before colliding elastically with a neutral in a momentum or charge exchange collision. Because the charge exchange cross section can substantially exceed the momentum exchange cross section, a probable result is that the ion becomes a fast neutral, and the neutral becomes positively charged and accelerates in the net $\boldsymbol{E}$ field. For the $E_r/B =$ constant situation, the degree of ionization rapidly goes to $nfe = 2.2$ (Fig. 15) and most heavy particles will be ionized.

The average result for an ion-neutral momentum collision is a loss of axial ion momentum and an equal axial momentum gain by the neutral. Since the ion initially has higher velocity its directed kinetic energy is collisionally converted to random thermal energy, increasing the heavy particle temperature and pressure. Calculation of this thermalization effect, which is strongest at low nfe, has not been attempted in this simplified model.

The ion-neutral interaction is further complicated by the finite size of the self-magnetic field region, in that an accelerating high-velocity ion, attempting to gyrate where the $B_\theta(z)$ field is weakening, may only complete a partial gyration before reaching $B = 0$. For the present example, for constant E_r at $u_2 = 36$ km/s, an ion at 24 km/s and $B/B_1 = 0.73$ is more than halfway through the sheet (Fig. 9) and has a Larmor radius and mean free path for C and F neutral elastic collisions approximately equal to the sheet width. At $u = 30$ km/s and $B/B_1 = 0.42$ the Larmor radius and mean free path are double the sheet width. At these velocities the remaining un-ionized neutrals do not affect the ion motion which becomes collisionless.

V. Conclusions

After more than 60 years of work with coaxial accelerators, new applications are being developed, particularly in the area of space propulsion such as the self-field MPD thruster. While advanced magnetohydrodynamic simulation codes such as PISO and MACH2, as well as advanced "black-box codes" (e.g., ANSYS), have been used successfully to provide detailed models of self-field [36] and applied-field [37,38] coaxial accelerators, the large parameter space means that these codes require significant time, effort, and experience to provide results for a wide range of operating conditions and geometries.

The approach of this paper is to provide an intentionally simplified model, but one that can be used as a comparatively agile and flexible analytic tool for examining performance limitations in coaxial geometries. This approach generates a guide to tradeoffs, their trends, and their influence on performance; a simplified characterization of the EM field and ion acceleration physics; and resulting guidance toward highly efficient plasma accelerators.

Using the simplified model, the calculated plasma parameters for a quasi-steady gas-fed coaxial self-field current sheet, for selected values of U_e, R_{oi}, and z_{12}, show that Teflon plasma ions are accelerated by an induced axial E_z electric field created by the Hall effect. Distribution of plasma parameters through the sheet depends strongly on the axial distribution (constant or decreasing) of the radial E_r field. At higher velocities the E_z field strengthens and the acceleration voltage across the current sheet exceeds the interelectrode voltage. The highest kinetic energy efficiency is achieved for the case of constant $E_r(z)$, and efficiency increases monotonically with sheet exit velocity.

The model has been applied to a Teflon ($C + 2F$) plasma exhaust beam with a velocity distribution determined by the masses and ionization potentials of the separate species. The model can be applied to single-species plasmas, which are expected to result in model predictions in closer agreement with exhaust beam properties.

If we evaluate the developed systems in Table 1 in terms of constant E_r or constant E_r/B, we find consistency with the model. The Teflon FPPT, for example, lacks a long central electrode, preventing it from displaying constant E_r operation, although mean plasma velocities up to 37 km/s can be achieved. The kinetic efficiency is only 14% (Table 1), consistent with the maximum predicted model value of 25% (Sec. III.B). The benchmark MPD using nitrogen propellant and possessing an extended central electrode achieves 40 km/s and a kinetic efficiency of 36% (Table 1). This value is well in excess of the model's 25% limit for constant E_r/B, so that the MPDT operates more like a constant E_r accelerator (Table 4). For these two examples, FPPT and MPDT, the operational values of E_r/B (43 and 25 km/s) are also consistent with constant E_r/B and constant E_r operation, respectively.

Still to be modeled is the effect of varying the electrode radius ratio by electrode tapering—converging as with the Cheng accelerator [6], diverging as with the FPPT accelerator [11,12] and MPD thruster [33], or a combination of constant diameter and diverging geometries. Future experimental efforts will accurately test the simplified model and predictions presented herein, and evaluate which of the more detailed physics issues require more attention.

Acknowledgments

This analysis work was supported by NASA Phase II SBIR Contract number 80NSSC18C0063 and CU Aerospace Internal Research and Development funds. The contract technical monitor was Richard Hofer of NASA's Jet Propulsion Laboratory. The authors thank Curtis Woodruff and Magdalena Parta of CU Aerospace for helpful discussions and assistance with model input information.

References

[1] Marshall, J., "Performance of a Hydromagnetic Plasma Gun," *Physics of Fluids*, Vol. 3, No. 134, 1960, pp. 134–135. https://doi.org/10.1063/1.1705989

[2] Aronowitz, L., and Duclos, D. P., "Characteristics of the Pinch Discharge in a Pulsed Plasma Accelerator," *ARS Electric Propulsion Conference*, AIAA, Reston, VA, March 1962, pp. 513–530. https://doi.org/10.2514/4.864865

[3] Ziemer, J. K., and Petr, R. A., "Performance of Gas Fed Pulsed Plasma Thrusters Using Water Vapor Propellant," AIAA Paper 2002-4273, July 2002. https://doi.org/10.2514/6.2002-4273

[4] Ducati, A. C., Giannini, G., and Muehlberger, E., "Experimental Results in High Specific Impulse Thermo-Ionic Acceleration," *AIAA Journal*, Vol. 2, No. 8, 1964, pp 1452–1454. https://doi.org/10.2514/3.2575

[5] Clark, K. E., and Jahn, R. G., "The Magnetoplasmadynamic Arcjet," *Astronautica Acta*, Vol. 13, No. 4, 1967, pp. 315–325.

[6] Cheng, D. Y., "Plasma Deflagration and the Properties of a Coaxial Plasma Deflagration Gun," *Nuclear Fusion*, Vol. 10, No. 3, 1970, pp. 305–317. https://doi.org/10.1088/0029-5515/10/3/011

[7] Burton, R. L., Clark, K. E., and Jahn, R. G., "Measured Performance of a Multimegawatt MPD Thruster," *Journal of Spacecraft and Rockets*, Vol. 20, No. 3, 1983, pp. 299–304. https://doi.org/10.2514/3.25596

[8] Choueiri, E. Y., and Ziemer, J. K., "Quasi-Steady Magnetoplasmadynamic Thruster Performance Database," *Journal of Propulsion and Power*, Vol. 17, No. 4, 2001, pp 967–976. https://doi.org/10.2514/2.5857

[9] Ziemer, J. K., Choueiri, E. Y., and Birx, D., "Is the Gas-Fed PPT an Electromagnetic Accelerator? An Investigation Using Measured Performance," AIAA Paper 1999-2289, 1999. https://doi.org/10.2514/6.1999-2289

[10] Laystrom, J., Burton, R., and Benavides, G., "Geometric Optimization of a Coaxial Pulsed Plasma Thruster," AIAA Paper 2003-5025, 2003. https://doi.org/10.2514/6.2003-5025

[11] Burton, R. L., Woodruff, C. A., King, D. M., and Carroll, D. L., "Analysis of Fiber-Fed Pulsed Plasma Thruster Performance," *Journal of Propulsion and Power*, Vol. 37, No. 1, 2021, pp. 176–178. https://doi.org/10.2514/1.B38114

[12] Woodruff, C. A., Parta, M., King, D. M., Burton, R. L., and Carroll, D. L., "Fiber-Fed Pulsed Plasma Thruster (FPPT) System with Multi-Axis Thrust Vectoring," *37th International Electric Propulsion Conference*, IEPC Paper 2022-558, June 2022.

[13] Paccani, G., Chiarotti, U., and Deininger, W. D., "Quasisteady Ablative Magnetoplasmadynamic Thruster Performance with Different Propellants," *Journal of Propulsion and Power*, Vol. 14, No. 2, March–April 1998, pp. 254–260. https://doi.org/10.2514/2.5275

[14] Thomas, R. E., Burton, R. L., and Polzin, K. A., "Performance Characteristics of an Ablative Gallium Electromagnetic Accelerator," *Journal of Propulsion and Power*, Vol. 3, No. 3, 2013, pp. 931–937. https://doi.org/10.2514/1.B34256

[15] Alfvén, H., *Worlds–Antiworlds: Antimatter in Cosmology*, W. H. Freeman, San Francisco, 1966, p. 74.

[16] Harte, J., *Consider a Spherical Cow*, Univ. Science Books, Melville, NY, 1988, p. 283, Chap. 1.

[17] Jahn, R. G., *Physics of Electric Propulsion*, McGraw–Hill, New York, 1968, pp 235–253.

[18] Burton, R. L., Rysanek, F., Antonsen, E. A., Wilson, M. J., and Bushman, S. S., "Pulsed Plasma Thruster Performance for Microspacecraft Propulsion," *Micropropulsion for Small Spacecraft*, edited by A. D. Ketsdever, and M. Micci, Vol. 187, Progress in Astronautics and Aeronautics, AIAA, Reston, VA, 2000, pp. 337–352. https://doi.org/10.2514/5.9781600866586.0337.0352

[19] Sutton, G. W., and Sherman, A., *Engineering Magnetohydrodynamics*, McGraw–Hill, New York, 1965, pp. 186–194.

[20] Sonoda, S., Henrikson, E., and Mikellides, P., "A High-Temperature, Thermal Non-Equilibrium Thermochemical Model for Polytetrafluoroethylene," *International Journal of Thermophysics*, Vol. 32, Sept. 2011, pp. 1918–1941. https://doi.org/10.1007/s10765-011-1030-y

[21] Richardson, A. S., *2019 NRL Plasma Formulary*, Naval Research Lab., Washington, D.C., 2019, p. 58.

[22] Zhong, J., Yang, F., Wang, W., Yuan, D., and Yan, J. D., "Net Emission Coefficient and Radiation Transfer Characteristics of Thermal Plasma Generated in Nitrogen-PTFE Vapor Mixture," *IEEE Transactions on Plasma Science*, Vol. 46, No. 4, 2018, pp. 990–1002. https://doi.org/10.1109/TPS.2018.2814399

[23] Liu, X., Wang, S., Zhou, Y., Wu, Z., Xie, K., and Wang, N., "Thermal Radiation Properties of PTFE Plasma," *Plasma Science and Technology*, Vol. 19, No. 6, 2017, Paper 064012. https://doi.org/10.1088/2058-6272/aa65e8

[24] Wang, H., Wang, W., Han, J. D., Qi, H., Geng, J., and Wu, Y., "Thermodynamic Properties and Transport Coefficients of a Two-Temperature Polytetrafluoroethylene Vapor Plasma for Ablation-Controlled Discharge Applications," *Journal of Physics D: Applied Physics*, Vol. 50, No. 39, 2017, Paper 395204.

[25] Seeliger, R., "Zur Deutung des Steenbeckschen Minimum Prinzips," *Zeitschrift für Physik*, Vol. 116, Nos. 3–4, 1940, pp. 207–213. https://doi.org/10.1007/BF01337385

[26] Finkelnburg, W., and Maecker, M., "Electric Arcs and Thermal Plasmas," *Encyclopedia of Physics, Gas Discharges II*, Vol. XXII, edited by S. Flugge, Springer, Berlin, 1956, p. 307ff.

[27] Li, H.-P., Pfender, E., and Chen, X., "Application of Steenbeck's Minimum Principle for Three-Dimensional Modelling of DC Arc Plasma Torches," *Journal of Physics D: Applied Physics*, Vol. 36, No. 9, 2003, pp. 1084–1096.

[28] Cohen, I. M., and Whitman, A. M., "On the Steenbeck Minimum Principle for Arc Discharges and Its Comparison with the Constant Property Arc," *Journal of Applied Physics*, Vol. 44, No. 4, 1973, pp. 1557–1561. https://doi.org/10.1063/1.1662411

[29] Benilov, M. S., and Naidis, G. V., "What Is the Mathematical Meaning of Steenbeck's Principle of Minimum Power in Gas Discharge Physics?" *Journal of Physics D: Applied Physics*, Vol. 43, No. 17, 2010, Paper 175204. https://doi.org/10.1088/0022-3727/43/17/175204

[30] Stratton, T. F., "High Current Steady State Coaxial Plasma Accelerators," *AIAA Journal*, Vol. 3, No. 10, 1965, pp. 1961–1963. https://doi.org/10.2514/3.3295

[31] McDonald, K. T., "Electron Trajectories in a Vacuum Coaxial Cable," Dept. of Physics, Princeton Univ., Princeton, NJ, http://physics.princeton.edu/∼mcdonald/examples/e_in_coax.pdf [updated 2008].

[32] King, D. Q., "Magnetoplasmadynamic Channel Flow for Design of Coaxial MPD Thrusters," Ph.D. Thesis, Dept. of Mechanical and Aerospace Engineering, Princeton Univ., Princeton, NJ, 1982.

[33] Jahn, R. G., *Physics of Electric Propulsion*, McGraw–Hill, New York, 1968, pp. 202–214.

[34] Ahlborn, B., "Approximate Calculation of the Speed of Sound in a Plasma," *Physics of Fluids*, Vol. 9, No. 9, 1966, pp. 1873–1874. https://doi.org/10.1063/1.1761951

[35] Burton, R. L., and Jahn, R. G., "Acceleration of Plasma by a Propagating Current Sheet," *Physics of Fluids*, Vol. 11, No. 6, 1968, pp. 1231–1237. https://doi.org/10.1063/1.1692090

[36] Xisto, C. M., Pascoa, J. C., and Oliveira, P. J., "Numerical Modelling of a Self-Field Magnetoplasmadynamic Thruster," *International Conference on Engineering ICEUBI2013, Conference Topic CT 2*, Univ. of Beira Interior, Covilha, Portugal, 2013.

[37] Mikellides, P. G., Turchi, P. G., and Roderick, N. F., "Applied-Field Magnetoplasmadynamic Thrusters, Part 1: Numerical Simulations Using the MACH2 Code," *Journal of Propulsion and Power*, Vol. 16, No. 5, Sept.–Oct. 2000, pp. 887–893. https://doi.org/10.2514/2.5656

[38] Haag, D., Fertig, M., and Auweter-Kurtz, M., "Numerical Simulations of Magnetoplasmadynamic Thrusters with Coaxial Applied Magnetic Field," *International Electric Propulsion Conference*, IEPC Paper 2007-138, 2007.

J. Blandino
Associate Editor